Elastic and Inelastic Mean Free Paths
for Scattering of Fast Electrons in Thin-Film Oxides

Adham Basha[1], George Levi[1], Tamir Amrani[1], Yang Li[2], Guy Ankonina[2], Pini Shekhter[3], Lior Kornblum[2], Ilan Goldfarb[1] and Amit Kohn[1*]

[1.] Department of Materials Science and Engineering, The Iby and Aladar Fleischman Faculty of Engineering, Tel Aviv University, Ramat Aviv, Tel Aviv 6997801, Israel.
[2.] Andrew and Erna Viterbi Faculty of Electrical and Computer Engineering, Technion – Israel Institute of Technology, 3200003 Haifa, Israel.
[3.] Tel Aviv University Center for Nanoscience and Nanotechnology, Tel Aviv University, Ramat Aviv, Tel Aviv 6997801, Israel.
* Corresponding author: akohn@tauex.tau.ac.il

Abstract

Quantitative transmission electron microscopy (TEM) often requires accurate knowledge of sample thickness for determining defect density, structure factors, sample dimensions, electron beam and X-ray photons signal broadening. The most common thickness measurement is by Electron Energy Loss Spectroscopy which can be applied effectively to crystalline and amorphous materials. The drawback is that sample thickness is measured in units of Inelastic Mean Free Path (MFP) which depends on the material, the electron energy and the collection angle of the spectrometer.

Furthermore, the Elastic MFP is an essential parameter for selecting optimal sample thickness to reduce dynamical scatterings, such as for short-range-order characterization of amorphous materials.

Finally, the Inelastic to Elastic MFP ratio can predict the dominant mechanism for radiation damage due to the electron beam.

We implement a fast and precise method for the extraction of inelastic and elastic MFP values in technologically important oxide thin films. The method relies on the crystalline Si substrate for calibration. The Inelastic MFP of Si was measured as a function of collection semi-angle (β) by combining Energy-Filtered TEM thickness maps followed by perpendicular cross-sectioning of the sample by Focused-Ion-Beam. For example, we measured a total Inelastic MFP (β~157 mrad) in Si of 145 ± 10nm for 200 keV electrons.

The MFP of the thin oxide films is determined by their ratio at their interface with Si or SiO_2. The validity of this method was verified by direct TEM observation of cross-to-cross sectioning of TEM samples. The high precision of this method was enabled mainly by implementing a wedge preparation technique, which provides large sampling areas with uniform thickness.

We measured the Elastic and Inelastic Mean Free Paths for 200keV and 80keV electrons as a function of collection angle for: SiO_2 (Thermal, CVD), low-κ SiOCH, Al_2O_3, TiO_2, ZnO, Ta_2O_5 and HfO_2.

The measured MFP values were compared to calculations based on models of Wenzel, Malis and Iakoubovskii. These models deviate from measurements by up to 30%, especially for 80keV electrons. Hence, we propose functional relations for the Elastic MFP and Inelastic MFP in oxides with respect to the mass density and effective atomic number, which reduce deviations by a factor of 2-3. In addition, the effects of sample cooling on the measurements and sample stability are examined.

Introduction

Thin-film oxides are a primary building block in many devices and have a wide range of state-of-the-art applications, such as optoelectronics, spin-electronics, energy harvesting and storage, memristive devices, and optical coatings [1–10].

Various methods are used for compositional and structural characterization of thin film oxides, for example: Raman spectroscopy, X-ray photoelectron spectroscopy, as well as X-ray, and neutron scattering [11]. However, for localized characterization of nanoscale volumes such as in thin films, Transmission Electron Microscopy (TEM) proves more effective due to the high scattering cross-section and small probe size of the electron beam [12,13].

Quantitative TEM requires accurate knowledge of sample thickness for determining properties such as defect density, structure factors, sample dimensions and geometry. Furthermore, an accurate measurement of the sample thickness is necessary for the modelling of image formation, estimation of electron beam or X-ray photon signal broadening, and evaluation of radiation damage [14–18].

Reported methods for direct measurement of the TEM sample thickness by a trigonometric-tilt series [19] and contamination-spot separation [20] suffer from complexity and poor accuracy. Convergent beam electron diffraction offers improved accuracy [21,22], but it is a very localized measurement, limited to crystalline materials, and more susceptible to beam damage [23]. Conversely, indirect thickness measurement using Electron Energy Loss Spectroscopy (EELS) or Energy-Filtered (EF) TEM can be applied effectively on both crystalline and amorphous materials [14–16,18,24–26]. The drawback is that sample thickness is measured in units of Inelastic Mean Free Path (MFP).

The Inelastic MFP value can be determined by calibrating EELS measurements using a perpendicular cross-section [16,24] or conical needle samples [14,27] prepared by Focused Ion Beam (FIB). However, these methods are limited since the MFP is measured per material and is dependent on several parameters, for example: Energy of the incident electron beam, and collection angle into the spectrometer. Consequently, reports on accurate measurements of elastic and inelastic MFP are limited [15,18,25,28–33].

The Elastic MFP is essential for determining the optimal sample thickness for structural short-range-order characterization of amorphous thin films [34]. The ratio of inelastic to elastic MFP is important to assess the dominant mechanism for radiation damage due to the electron beam: atom displacement or radiolysis [35]. The sample thickness in units of Elastic MFP can be measured from the zero-loss peak intensity in nano-diffraction patterns on the sample compared to vacuum [24], or alternatively, using the EELS log-ratio technique on EF-TEM images with a combination of a small objective aperture (<2mrad) to exclude all types of scattered electrons [36]. As for the case of the Inelastic MFP, extracting the Elastic MFP value requires accurate knowledge of the sample thickness. We note that reports on Elastic MFP values are scarce in the literature.

To date, MFP values were not reported for many technologically important thin-film oxides such as Ta_2O_5, HfO_2, Al_2O_3, TiO_2, ZnO and low-κ porous SiO_2 (SiOCH). When MFP values are reported, they are typically stated for a specific collection angle or electron energy. In addition, while Inelastic MFP values for SiO_2 were reported previously [15,37], the influence of the synthesis method of the film (thermal/CVD) on the MFP values was not examined.

In this work, we implement a straightforward calibration methodology for determining the inelastic and elastic MFP of 200keV and 80keV electrons in technologically important thin film oxides deposited on

high-quality single-crystal semiconductors, typically silicon. This method is based on accurate measurement of the Inelastic MFP of electrons in crystalline silicon using indirect EF-TEM thickness mapping followed by FIB perpendicular cross-sectioning of TEM samples. Based on this calibration, the MFP is determined for the oxide thin films deposited on Si/SiO_2 substrates by measuring the thickness ratio in MFP units at interfaces which are of the same physical thickness.

We compare the measured MFP to calculated values using the Wenzel, Iakoubovskii and Malis models for elastic and inelastic scattering, respectively [18,28,29,38]. We propose functional relations on the Elastic MFP and Inelastic MFP in oxides with respect to the mass density and effective atomic number. In addition, the effects of sample cooling on the measurements and sample beam damage are examined.

Experimental procedure

Materials

Oxides thin films were prepared as follows:

Amorphous SiO_2 film (nominal thickness of 300nm) was prepared by dry thermal oxidation on Si(001) substrates, supplied by UniversityWafer, Inc.

Amorphous Ta_2O_5 (nominal thickness of 250nm) thin film was prepared by RF magnetron sputtering from a metallic Ta target at room-temperature, working vacuum pressure of 3.75 mTorr, 150W and 30% oxygen flow using a PVD4 system of VINCI™ technologies.

Amorphous Al_2O_3 thin film (nominal thickness of 20nm) was grown by atomic layer deposition using Ultratech/Cambridge Nanotech Fiji G2 at 300 °C using trimethyl-aluminum (TMA) and water as the Al and the oxygen precursors, respectively[39]. One cycle of Al_2O_3 deposition consists of 0.1s TMA injection, 10s Ar gas purge, 0.3s H_2O injection, and 5s Ar gas purge. In total, 200 Al_2O_3 deposition cycles are used.

Amorphous HfO_2, TiO_2 and polycrystalline ZnO thin films (nominal thickness of 15-20nm) were prepared by sputtering at room-temperature using an ATC 2200 system (AJA International Inc.) holding metal oxide targets (99.99% purity). The Ar/O_2 gas mixture was supplied at 50:5 sccm at a process pressure of 3 mTorr. The oxide films were capped *ex-situ* with an Al layer (nominal thickness of 50nm) deposited using e-beam deposition (Evatec BAK-501A) at room temperature.

All the oxide thin films were deposited onto a Si(001) substrate covered with a plasma-enhanced chemical vapor deposition (PECVD) SiO_2 layer deposited at 573K (nominal thickness of 60-100nm).

In addition, commercially available (TSMC) low porosity carbon doped low-κ SiOCH (κ~2.6, n~1.4) film with nominal thickness of 300nm and Si:C:O atomic ratio of 1:1:2 was deposited using PECVD on a n-type Si(001) substrate.

Methods

The composition and chemical bonding of the oxides were verified by X-ray photoelectron spectroscopy (XPS) using a Versaprobe III and Multi-Technique System 5600 (PHI, USA). A monochromatic Al Kα source (1486.6eV) produced an X-Ray beam with a diameter of 200 μm. The measurements were performed in an UHV ($2x10^{-10}$ Torr) analysis chamber. Spectra were shifted to adventitious C1s peak at 284.8eV. Precise energy positioning and peak shape determination was achieved from individual spectrum measurement for different peaks in a small energy range window at a high resolution (PE = 11.75 eV, 0.1 eV/step). The extracted oxide compositions are presented in the supplementary information.

The mass densities of the oxide films were measured by X-ray reflectivity (XRR) using Rigaku SmartLab 9kW Cu anode X-ray diffractometer equipped with Ge220x2 monochromator and operated at 45kV (200 mA). XRR data was fitted to calculated curves using GlobalFit2.0 and SmartLab studio II softwares by Rigaku. Film thicknesses measured from bright-field (BF) TEM micrographs were used to improve the fitting accuracy and to refine the measured density values. (Supplementary – Fig. S3).

TEM cross-sectional samples were prepared by a wedge preparation method [40]: The sample is glued to a protective silicon (001) wafer slide and mechanically polished down to thickness of 1-5 µm at the region of interest using a MultiPrep™ system (Allied High Tech, USA) while applying a wedge angle of ~1-2˚ as shown in the schematic Fig. 1. Mechanical polishing is followed by a short period of Ar ion milling using PIPS II (Gatan, USA) at energies ranging from 4 keV down to 0.2 keV while cooling the sample to a temperature of 200K for minimizing damage induced by the ion polishing process. Subsequent measurement of the wedge angle resulted in 3-8°, attributed to the final ion polishing stage.

The thickness of the TEM samples in units of electron mean free path, inelastic or elastic, was determined from Energy-Filtered (EF) TEM images using intrinsic electron scattering lengths based on Poisson statistics, resulting in a log-ratio equations, (Eq. 1a) for inelastic scattering and (Eq.1b) for elastic scattering [18]:

$$\frac{t}{\lambda_{inelastic}} = \ln(\frac{I_t}{I_0}) \tag{1a}$$

where t is the sample thickness, $\lambda_{inelastic}$ is the inelastic scattering MFP, I_0 is the intensity of the zero-loss image (intensity of electrons transmitted without energy-loss), and I_t is the total intensity without energy filtering, which is equivalent to the intensity of an entire EEL spectrum for a given collection semi-angle, β.

For the elastic scattering MFP, $\lambda_{elastic}$:

$$\frac{t}{\lambda_{elastic}} = \ln(\frac{I_0}{I_u}) \tag{1b}$$

where I_u is the image intensity of the un-scattered electrons, achieved by inserting the smallest objective aperture available (5µm in diameter), equivalent to 2mrad angular spread, to the zero-loss images. The combination of the 10eV energy slit and 2mrad objective aperture excludes the majority of both inelastically and elastically scattered electrons [36].

The accuracy of this approach can be estimated, in the case of elastically scattered electrons, by the Wentzel model, presented in the supplementary information. For I_0, the objective lens bore of the TEM [36] or the differential pumping aperture between the specimen chamber and the projector lens limits the collection angle of scattered electrons. In the case of the microscope used for this research, the angle limit is up to approximately 157mrad [23]. Thus, the largest error occurs for the larger electron wavelength (80keV energy) and highest effective atomic number (HfO_2), resulting in up to 6% of the electrons that can be elastically scattered to an angle beyond 157mrad. For I_u, the smallest objective aperture is limited to approximately 2mrad. Thus, the largest error occurs for the smaller electron wavelength (200keV energy) and smallest effective atomic number (SiO_2), resulting in up to 1% of the electrons that can be elastically scattered in this small angular range. For I_0, some inelastically scattered electrons can enter the 10eV energy selecting slit, which we estimate at below 3%.[36]

Energy-filtered (EF) TEM thickness maps of areas with thicknesses between 0.2 and 1 t/IMFP of the thin film oxides were acquired for 80keV and 200keV electrons using a JEOL JEM 2010F TEM. The thickness maps were acquired with parallel illumination (α~0.2mrad), 10eV energy slit and collection semi-angles between 2 and 157 mrad using a US1000 CCD detector at the back of a Gatan Imaging Filter (Tridiem). To reduce beam damage and hydrocarbon contamination, some of the experiments were performed under sample cooling (temperature of ~90K), However, even at room-temperature measurements, investigating the EF-TEM images of the samples pre and post exposure show no evidence for hydrocarbon contamination build-up or shrinkage of the oxide films.

For calibration purposes, the Inelastic MFP values of 200keV and 80keV electrons in crystalline Si(001) as a function of the spectrometer collection semi-angle were determined to an accuracy of a few nanometres. This calibration was performed as follows: Acquisition of EF-TEM thickness maps of several Si(001) samples prepared by Focused Ion Beam (FEI Helios NanoLab 460F1 DualBeam FIB) in order to achieve uniform sample thickness. Following this, direct thickness measurements by cross-to-cross sectioning of the sample, again by FIB. Finally, the spectrometer collection semi-angles were calibrated using diffraction patterns from the Si substrate to determine the angular diameter of the objective apertures. (Supplementary – Fig. S1).

The thickness and consequently the MFP values of the oxide films were determined at the Si/Oxide interface using the well calibrated Si Inelastic MFP values. The validity of this ratio method at Si/Oxide interfaces was verified by FIB perpendicular cross sectioning of Si/Oxide TEM samples. Examination in the TEM of these cross-to-cross sectioned samples proved the assumption of equal thickness of the Si substrate and the oxide film adjacent to the interface. For example, Fig. 2 shows a secondary electron (SE) scanning electron microscopy (SEM) image of such a sample.
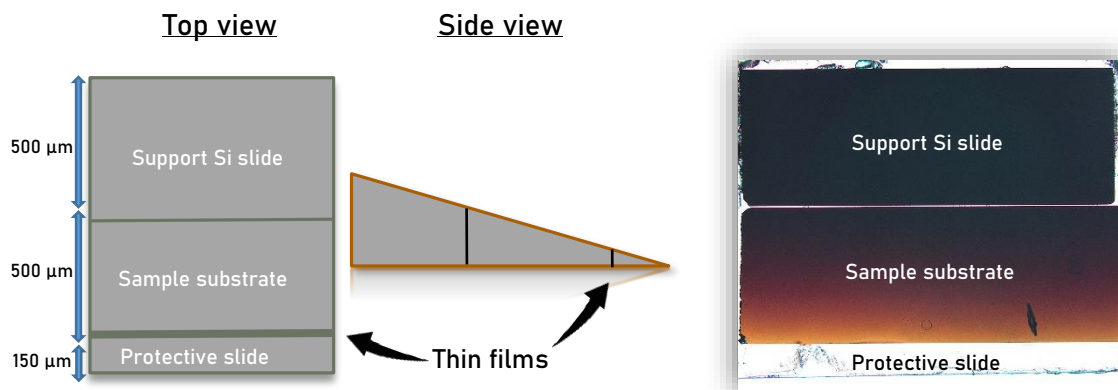

Figure 1. (Left) Schematic of a wedge TEM sample structure: The thin films are protected with a silicon, or a glass slide and the substrate is supported by an additional silicon wafer slide. (Right) Optical micrograph (bottom illumination) of a wedge TEM sample prior to ion polishing. The red hue indicates a silicon region of approximately 5μm thickness or less.

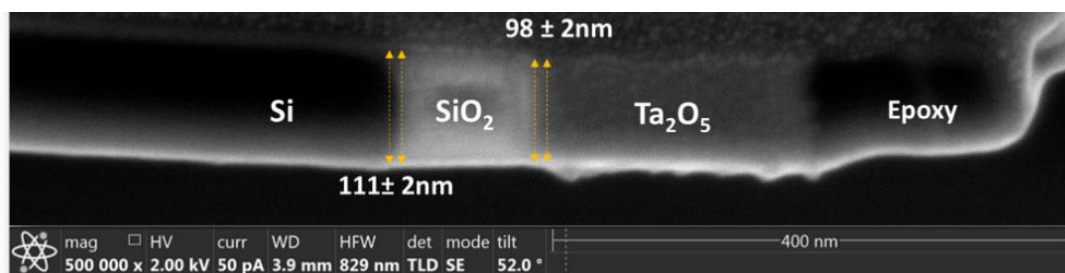Figure 2. SE SEM image of a cross-to-cross FIB section from a Si/SiO$_2$/Ta$_2$O$_5$ sample. The sample thickness is uniform adjacent to interfaces, thus verifying extraction of MFP values by a ratios approach with respect to the calibrated silicon value.

Results and discussion

1. Calibration: The inelastic MFP of silicon

The BF TEM micrographs in Fig.4 show examples of the layer arrangement of the investigated samples. Fig. (3a) shows a thermally oxidized SiO_2 thin film on a Si(001) substrate, Figs. (3b) and (3c) show amorphous Ta_2O_5 and HfO_2 films, respectively, deposited on a Si(001) substrate covered with PECVD SiO_2.
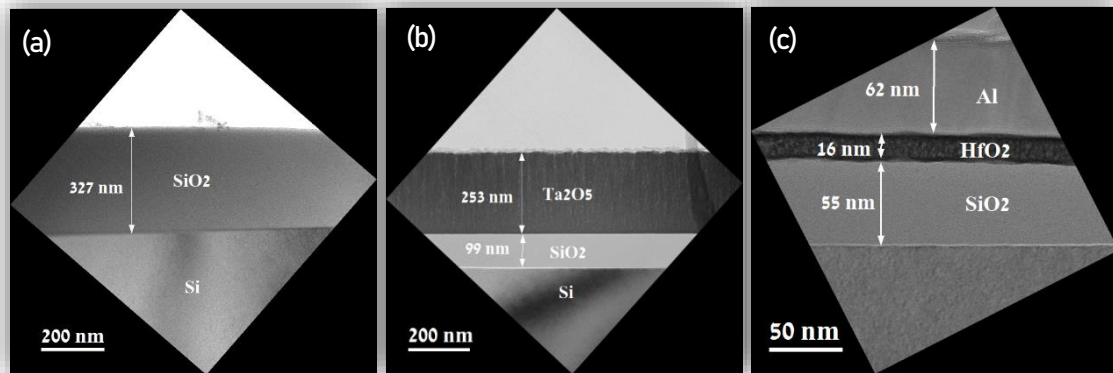

Figure 3. BF TEM cross-sectional micrographs, overview of (a) dry-thermal SiO_2 film (~330nm) grown on a Si (001) substrate, (b) Ta_2O_5 film (~250nm thick) deposited on a SiO_2 (~100nm thick)/Si (001) substrate and (c) HfO_2 film (~16nm thick) deposited on a CVD SiO_2 (~55nm thick)/Si (001) substrate and capped with Al layer (approximately 60nm thick).

The above-mentioned thin film oxides are deposited on high quality single crystal silicon substrates, as is the case for many devices [7,41–47]. Therefore, in the following implemented method, we obtain an accurate measurement of the Inelastic MFP of fast electrons in crystalline silicon using EF-TEM thickness mapping of FIB prepared Si samples with a range of thicknesses. These measurements are used as a built-in calibration reference for determining the thickness of the oxide films adjacent to the interfaces and consequently their inelastic and elastic MFP values.

Fig. (4a) shows, as an example, SE-SEM images of a FIB prepared lamella of crystalline silicon covered with thermal SiO_2. The sample was thinned using the Ga ion beam down to a thickness of approximately 50nm as shown in the side view SE-SEM image in Fig. (4b). An accurate determination of the thickness was done using BF TEM (e.g., Fig.6a). A thickness map in units of Inelastic MFP using EF-TEM was acquired from each sample as seen for example in Fig. (5a). Average thickness profiles were acquired from the Si substrate adjacent to its interface with the oxide as shown in Fig. (5b). This was followed by preparation of a perpendicular FIB cross-section (cross-to-cross) from each sample for direct thickness measurements of the silicon substrate at the Si/Oxide interface as shown in Fig. (6a).
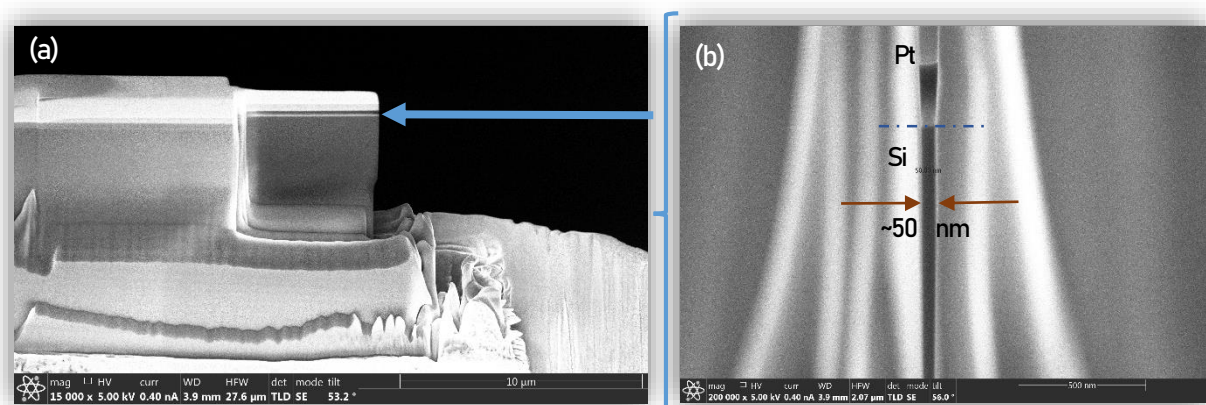

Figure 4. (a) Top view and (b) side view of a SE SEM image of Si/SiO₂ FIB prepared TEM sample with a nominal thickness of 50nm. (For accurate thickness measurement see Fig.6a).
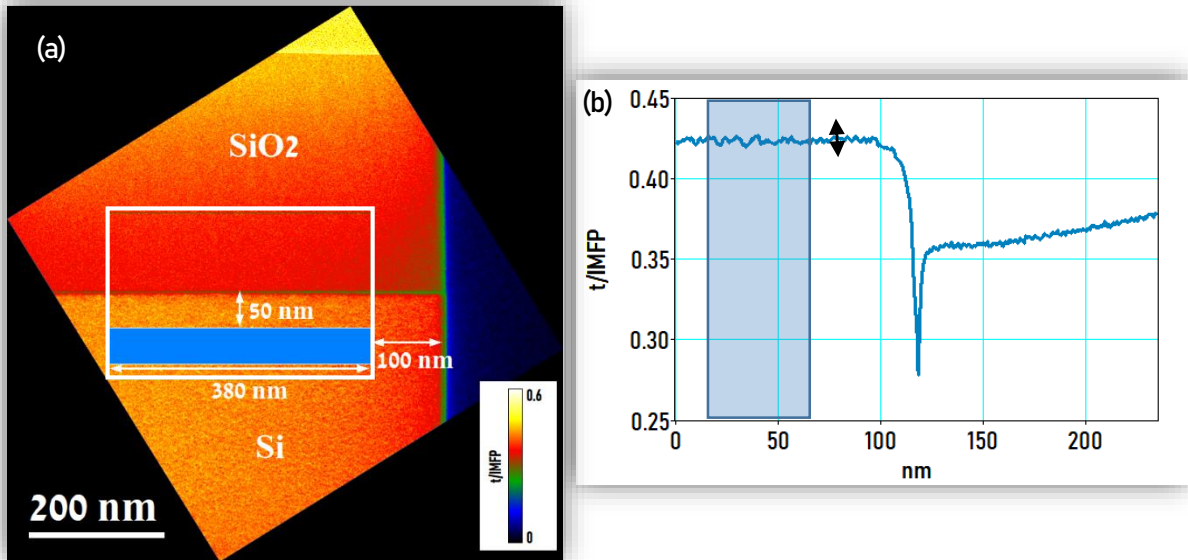
Figure 5. (a) Thickness map in units of Inelastic MFP (β~157mrad) obtained from Energy-filtered TEM measurements of a Si/SiO₂ FIB cross-sectional sample (b) Average thickness profile (left to right) in units of Inelastic MFP acquired from the area denoted by the white rectangle (bottom to top) in (a), using an integration width equal to the width of the box. The average thickness profile of Si was acquired from the area denoted by the blue rectangle (the area is slightly distant from the sample edge and oxide interface to avoid imaging artefacts).

The above procedure was carried out following measurements with 80keV and 200keV electrons and spectrometer collection semi-angles ranging from 2 to 157 mrad on three Si samples with different thicknesses. The varying thicknesses enable the extraction of the MFP values at improved accuracy, while reducing the contribution of the damaged outer layer, due to the FIB preparation process. The error was estimated from the standard deviation of the relative thickness ($t/\lambda_{inelastic}$) and the actual thickness measurements. In addition, system noise of up to 0.03 ($t/\lambda_{inelastic}$) for β~157mrad was estimated and accounted for by measuring an average thickness profile in the vacuum at a distance of several tens of nanometres away from the sample.

The resulting Inelastic MFP values of crystalline Si (oriented close to Z.A [110]) are shown in Fig. (6b) and are summarized in Table 1. The measured values for 200keV electrons are consistent to previously reported values [15,16,23,31,48]. No previous reports for Inelastic MFP of 80keV electrons were found for comparison.
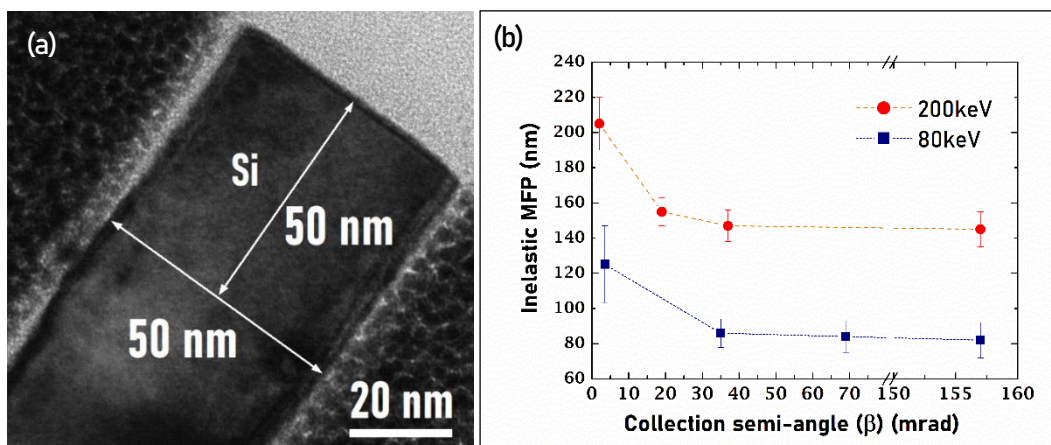

Figure 6. (a) BF TEM micrograph of a Si/SiO₂ perpendicular FIB cross-section (cross-to-cross) acquired from one of the samples previously measured using EF-TEM with 200keV electrons. The arrows represent the measurement of sample thickness and position of the EF-TEM measurements. This TEM micrograph enables calibrating the thickness maps by direct measurement of the Si substrate thickness. (b) Measured values of Inelastic MFP of 80keV and 200keV electrons in crystalline Si(close to Z.A. [110]) as a function of the spectrometer collection semi-angle (β). Dotted lines are guides for the eye.

7

Table 1. Inelastic MFP of crystalline Si (close to Z.A. [110]) measured for 200keV and 80keV electrons as a function of the collection semi-angle (β)				
	~157 mrad	36 ± 1 mrad	19 ± 0.5 mrad	2 ± 0.5 mrad
Inelastic MFP at 200 kV (nm)	145 ± 10	147 ± 9	155 ± 8	208 ± 15
Inelastic MFP at 80 kV (nm)	82 ± 4	86 ± 6	89 ± 5	125 ± 12

2. Inelastic and Elastic MFP in oxide thin films

Based on the calibration process described in the above section, we can determine the actual thickness of the Si substrate in any of the TEM wedge samples and consequently determine the thickness of the oxide film deposited on Si. As an example, Fig. (7a) shows an EF-TEM thickness map in Inelastic MFP units of a Si/SiO$_2$/HfO$_2$/Al TEM sample acquired using an energy slit of 10eV and collection semi-angle of β~157 mrad (without an objective aperture). Using the Si Inelastic MFP calibration, the thicknesses of the Si substrate and adjacent oxide layers, were determined from the average thicknesses of the marked regions (1-4) (Fig. (7b)).

Similarly, thickness maps in units of elastic MFP for electron scattering were generated from the exact same regions in each sample as shown, for example, in Fig. (7c, d). Dividing the thickness of every film by the average t/IMFP profile in each region enables the extraction of the Elastic and Inelastic MFP values of the oxide films as a function of the electron energy and collection angle.

The TEM sample preparation technique adopted for these samples (see methods section), yields several vast electron-transparent regions with uniform thickness, each stretching for several microns along the Si-Oxide interface. Such large electron-transparent regions enable repeating the above procedure on many locations across each sample and thus averaging the measured thickness profile to improve the precision of the method.

We note that the average t/IMFP values were not measured directly at the interfaces to reduce the effects of imaging artefacts due to imperfect image alignment and variation in the oxide film density close to the interfaces. Furthermore, for the IMFP measurements, we tilted the sample slightly away from zone-axis at less than 2°. Following this tilt, we did not notice effects of dynamical scattering near the Si/Oxide interface.

When attempting to measure the Elastic MFP in the crystalline Si substrate, we did notice channeling and dynamical scattering effects. Therefore, we do not report Elastic MFP of crystalline Si. However, this lack of Elastic MFP calibration does not affect the measurements of the amorphous/polycrystalline thin-films, since the sample thickness is calibrated using the IMFP of Si near the interface.
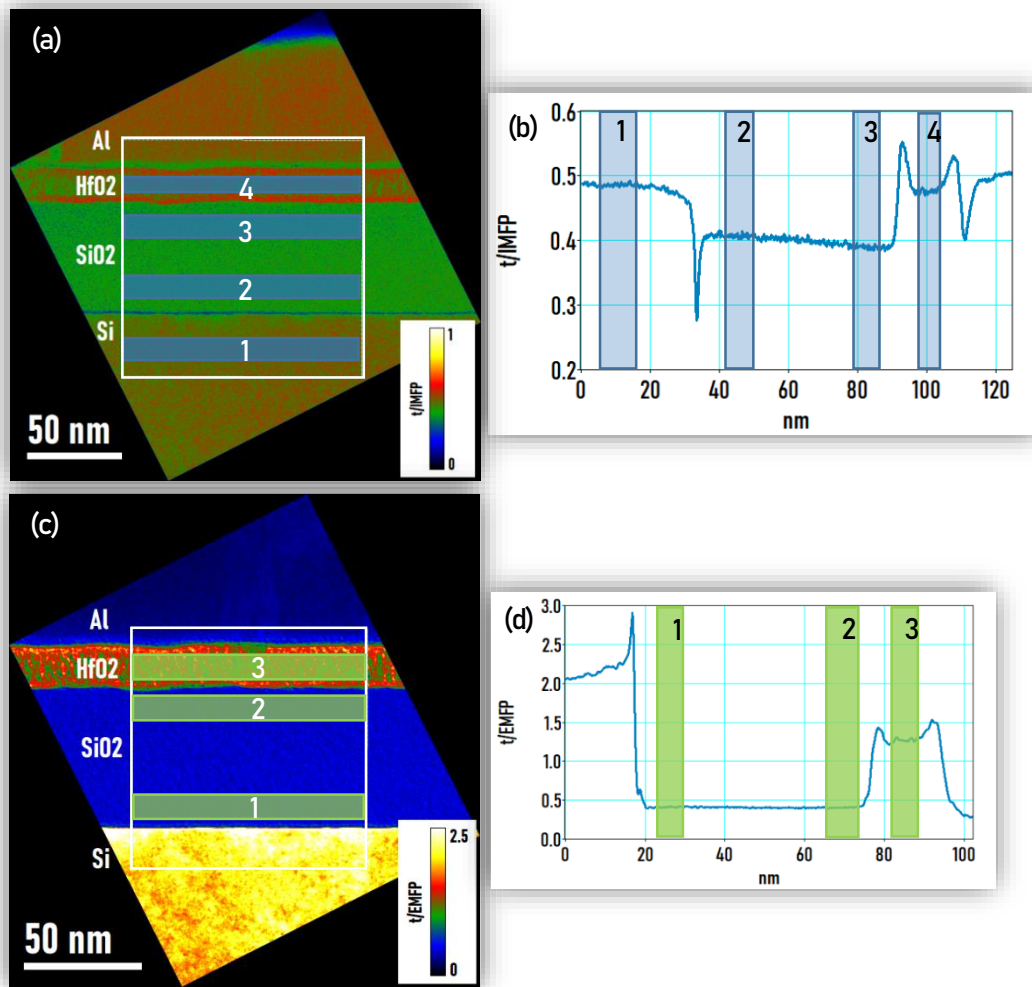
Figure 7. (a) EF-TEM thickness map in t/IMFP units of a Si/SiO$_2$/HfO$_2$/Al wedge sample acquired using an energy slit of 10eV and collection semi-angle of $\beta\sim$157 mrad. (b) Average thickness profile in units of Inelastic MFP acquired from the area denoted by the white rectangle in (a). The film thicknesses were calculated in areas (1-4) denoted by the blue rectangles using the Si Inelastic MFP calibration. (c) EF-TEM thickness map in t/EMFP units of the same sample acquired using an energy slit of 10eV and objective aperture of 2mrad. (d) Average thickness profile in units of t/EMFP acquired from the area denoted by the white rectangle in (c). The Elastic MFP values were extracted by dividing the average t/EMFP thickness profile in each area (denoted by the green rectangles) by the actual film thicknesses which was determined previously using the Si Inelastic MFP calibration.

Fig. (8a, 8b) show examples of calibrated sample thicknesses with respect to the average t/IMFP thickness profile in CVD SiO$_2$ and in Ta$_2$O$_5$, measured at different electron energies and collection semi-angles. The plots were fitted linearly, and the intercept with the thickness axis (y-axis) was constrained at zero, in order to limit the influence of surface plasmons on the measured relative thickness of the thin regions on the sample (<0.4 $t/\lambda_{inelastic}$). The Inelastic MFP values were extracted from each of the slopes as shown in Fig. (8c).

As examples of extraction of Inelastic MFP values, the measured $\lambda_{inelastic}$ for 200keV electrons in SiO$_2$ is 170 ± 8nm and 178 ± 10nm for a collection semi-angle of $\beta\sim$157 mrad and $\beta\sim$19 mrad, respectively, in agreement with previously reported measurements and calculations [15,49,50]. For Ta$_2$O$_5$, the measured total (i.e., $\beta\sim$157 mrad) $\lambda_{inelastic}$ was 128 ± 12nm and 84 ± 5nm for 200keV and 80keV electrons, respectively. These parameters have not been reported previously.
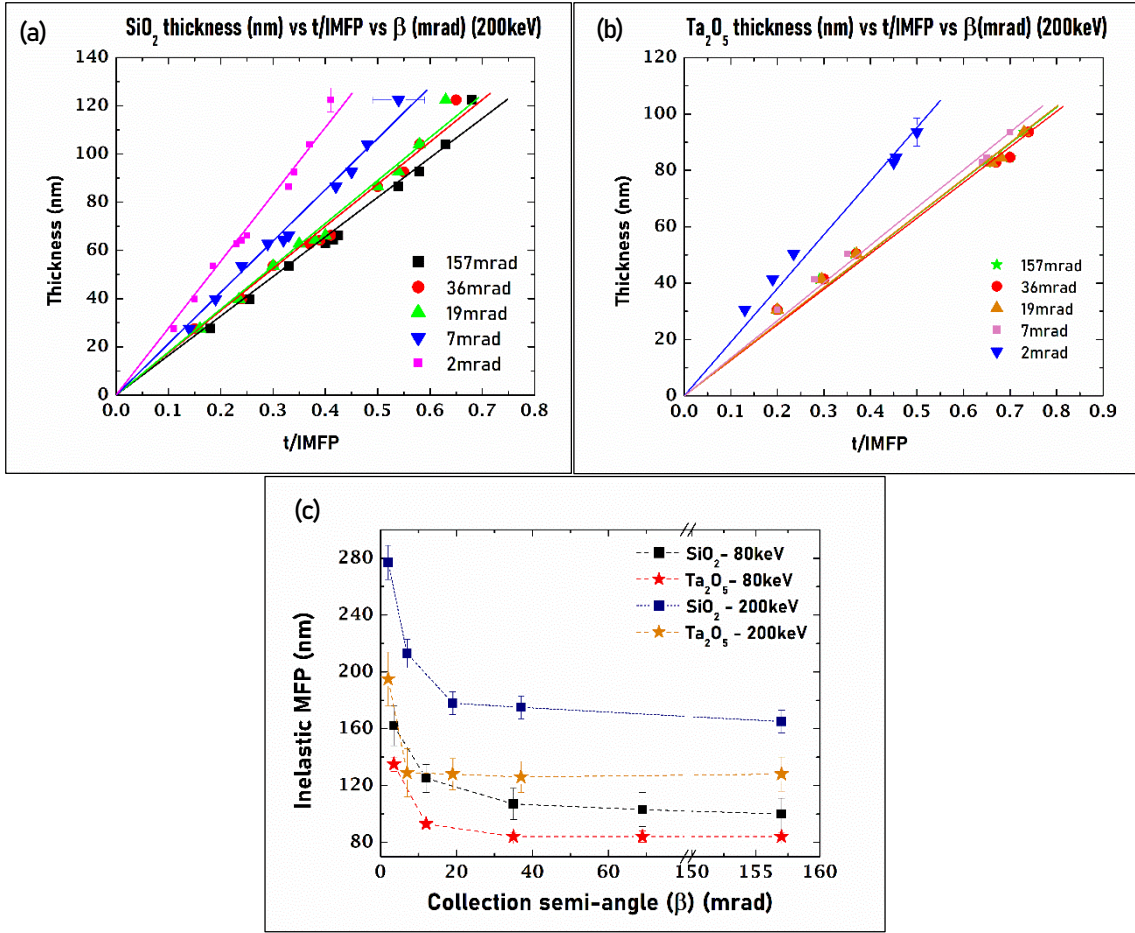
Figure 8. Thickness of the TEM sample in the region of (a) thermal SiO$_2$ and (b) Ta$_2$O$_5$ thin films at different locations across each sample as a function of the measured t/IMFP of 200keV electrons for a range of collection semi-angles. From each slope, $\lambda_{inelastic}$ is extracted for the specific collection semi-angle. (c) Measured values of Inelastic MFP of 80keV and 200keV electrons ($\lambda_{inelastic}$, $\lambda_{elastic}$) in thermal SiO$_2$ and Ta$_2$O$_5$ thin films as a function of the collection semi-angle (β). Dotted lines are guides for the eye.

This above procedure was repeated for all the oxide-thin films both for Elastic and Inelastic t/MFP thickness maps acquired for 80keV and 200keV electrons. The measured Inelastic MFP values for each oxide thin film as a function of the collection semi-angle (β) are shown in Fig.9. The total Elastic and Inelastic MFP values are summarized in Table 2 and Table 3, respectively. The value of $\lambda_{inelastic}$ typically decreases to a steady-state value at collection semi-angles above 20mrad for all oxides with a steady decrease in the MFP as a function of the material density.

The relative errors calculated for the Elastic and Inelastic MFP of the oxide films measurements are 5-7% both for 200keV and 80keV electrons. These errors were calculated from the statistical standard deviation of measurements collected at different locations, typically 6-8, on the sample with varying thicknesses. We believe that this relative error can be further reduced by increasing the number of measured locations and thicknesses and by increasing the count rates using multiple EF-TEM exposures or alternatively, Scanning TEM EELS line scans across the sample.

In addition, the Elastic and Inelastic MFP values for thermal SiO$_2$ and CVD SiO$_2$ are almost identical, which was expected due to the similarity of measured density and stoichiometry of both films. The total Inelastic MFP values for 200keV electrons in CVD SiO$_2$ and for Al$_2$O$_3$ were also consistent with a previous report by Iakoubovskii [37].

10

We note that the ZnO thin film was polycrystalline, as opposed to the other oxide thin-films which were amorphous. Nevertheless, we were able to extract the MFP values by averaging the thickness profile across large regions including many grain orientations, thus averaging contributions of dynamical scattering from grains oriented close to zone axis.
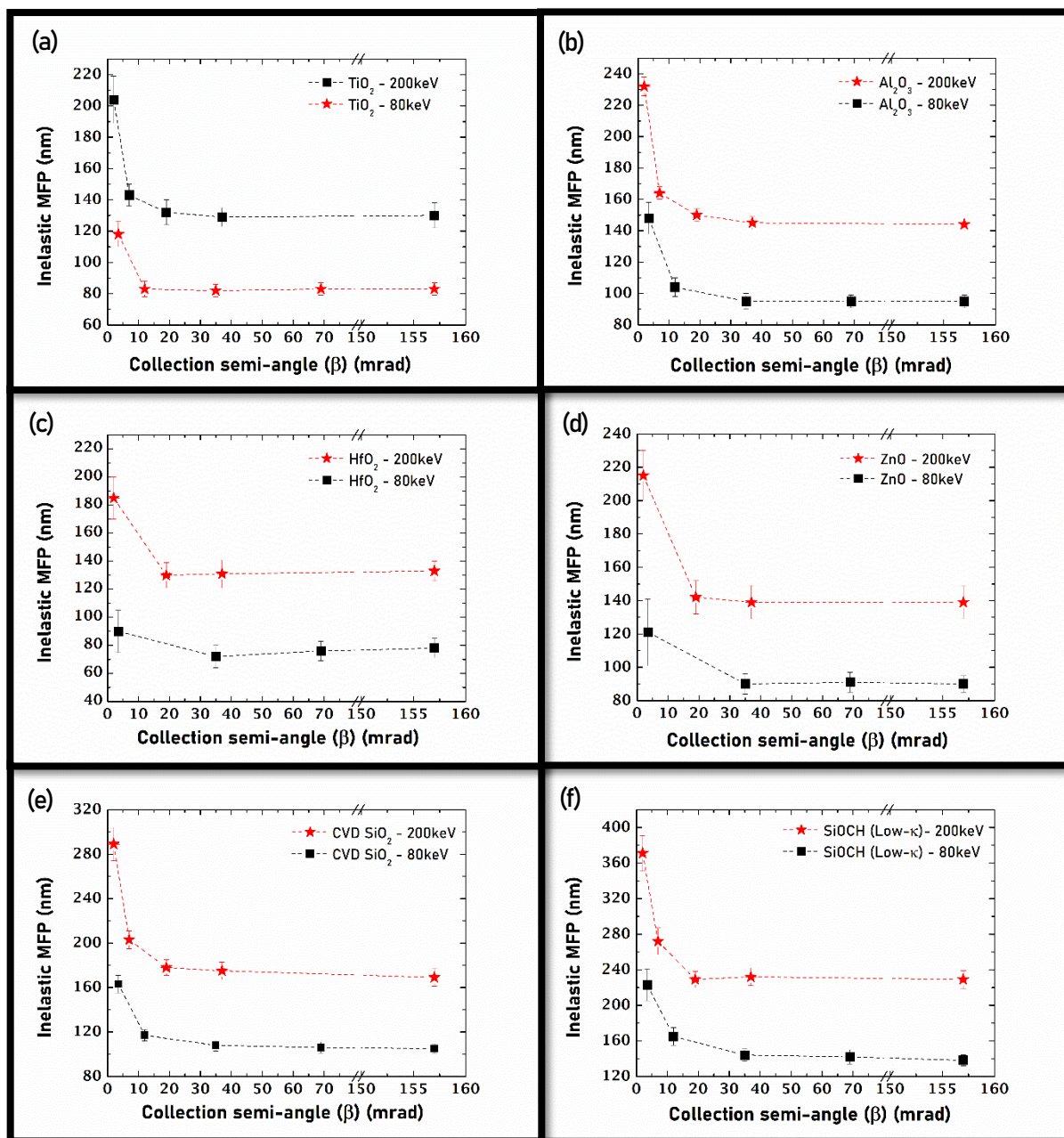

Figure 9. Measured Inelastic MFP values for 200keV and 80keV electrons in (a) TiO$_2$ (b) Al$_2$O$_3$ (c) HfO$_2$ (d) ZnO (e) CVD SiO$_2$ and (f) Low-κ SiOCH as a function of the collection semi-angle (β). Dotted lines are guides for the eye.

Table 2. Total Elastic MFP values of 200keV and 80keV electrons in examined oxide thin films

Oxide	Density (g/cc)	Elastic MFP – 200keV (nm)	Elastic MFP – 80keV (nm)
SiO_2 (Thermal)	2.2 ± 0.1	172 ± 10	107 ± 6
SiO_2 (CVD)	2.2 ± 0.1	173 ± 11	107 ± 5
SiOCH (Low-κ)	1.5 ± 0.1	240 ± 16	133 ± 10
Al_2O_3	3.2 ± 0.1	170 ± 8	111 ± 7
TiO_2	3.9 ± 0.1	106 ± 6	65 ± 4
ZnO	5.6 ± 0.1	81 ± 10	56 ± 12
Ta_2O_5	6.9 ± 0.1	46 ± 4	31 ± 3
HfO_2	7.7 ± 0.1	50 ± 4	34 ± 4

Table 3. Total Inelastic MFP values of 200keV and 80keV electrons in examined oxide thin films

Oxide	Inelastic MFP – 200keV (nm)	Inelastic MFP – 80keV (nm)
SiO_2 (Thermal)	168 ± 8	100 ± 11
SiO_2 (CVD)	169 ± 8	105 ± 5
SiOCH (Low-κ)	229 ± 10	138 ± 6
Al_2O_3	144 ± 6	95 ± 5
TiO_2	130 ± 8	83 ± 5
ZnO	139 ± 10	90 ± 6
Ta_2O_5	128 ± 12	84 ± 5
HfO_2	133 ± 7	78 ± 7

The effect of sample cooling to liquid nitrogen temperature (~80K) on the MFP measurements is demonstrated in Fig. 10 for thermal SiO_2 and Ta_2O_5. While thermal diffuse scattering is not expected to affect significantly these measurements, sample cooling was beneficial in reducing beam damage, especially at the lower electron energy of 80keV. Indeed, no significant effect on the measured Inelastic or Elastic MFP values was observed.
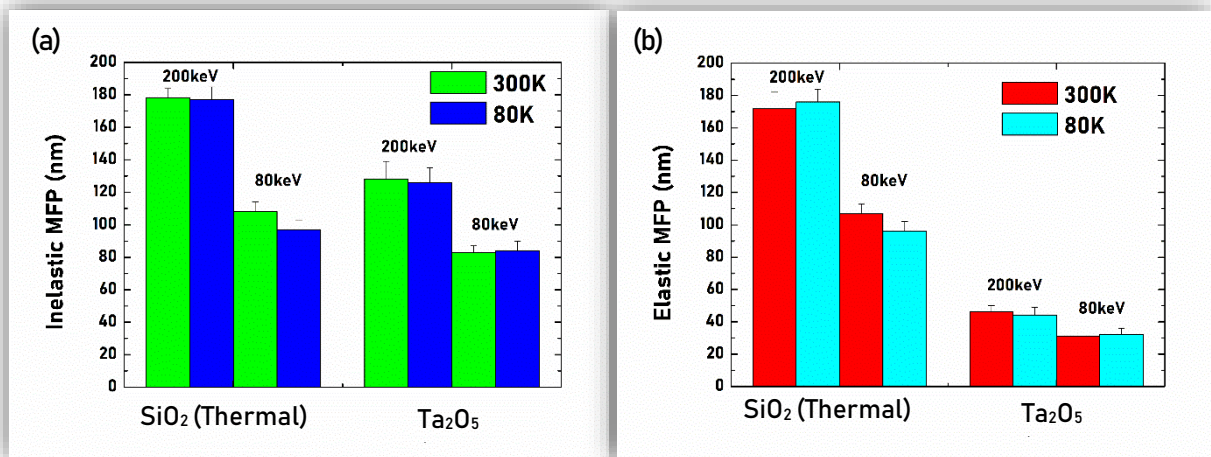

Figure 10. (a) Partial Inelastic (collection semi-angle of ~20mrad) and (b) Total Elastic MFP for 200keV and 80keV electrons as a function of sample cooling to liquid nitrogen temperature (~80K).

3. Comparison of measured Inelastic and Elastic MFP to models

3.1 Inelastic MFP

A semi-empirical model to calculate the Inelastic MFP was proposed by Malis *et al.* [18] and Egerton *et al.* [51] (Eq.2):

$$\lambda_{inelastic} = \frac{106F\left(\frac{E_0}{E_m}\right)}{\ln\left(\frac{2E_0\beta}{E_m}\right)} \ [nm] \tag{2}$$

Where E_0 is the electron beam energy (keV), $F = \frac{1+\frac{E_0}{1022}}{\left(1+\frac{E_0}{511}\right)^2}$ is a relativistic factor , β is the collection semi-angle (mrad) and E_m is the most probable energy loss for inelastic scattering (eV), which can be estimated by [Eq. 3] [17]:

$$E_m = 7.6Z^{0.36} \tag{3}$$

Where Z is the atomic number of the element under measurement.

If the sample is a compound, then Z is replaced by an effective atomic number, $\frac{\Sigma_i f_i Z_i^{1.3}}{\Sigma_i f_i Z_i^{0.3}}$, for which f_i is the atomic fraction of element *i* in the material. [18]

A second semi-empirical approach to estimate the Inelastic MFP, [Eq. 4], was introduced by Iakoubovskii *et al*. This model also accounts for the material density and the convergence angle of the incident electron probe [29]:

$$\lambda_{inelastic} = \frac{200FE_0}{11\rho^{0.3}\ln\{(\alpha^2 + \beta^2 + 2\theta_E^2 + |\alpha^2 - \beta^2|)/(\alpha^2 + \beta^2 + 2\theta_C^2 + |\alpha^2 - \beta^2|)x\left(\frac{\theta_C^2}{\theta_E^2}\right)\}} \tag{4}$$

Where ρ is the sample mass density $(\frac{gr}{cm^3})$, α is the beam convergence semi-angle, $\theta_c = 20 mrad$ and $\theta_E = \frac{5.5\rho^{0.3}}{FE_0} \ (mrad)$ is the characteristic angle for scattering.

Fig.11 shows a comparison of measured and calculated values of partial inelastic MFP ($\beta \sim 20 mrad$ for 200kV and $\beta \sim 35 mrad$ for 80kV) to the Malis and Iakoubovskii models. The Inelastic MFP values for 200keV electrons calculated using the Iakoubovskii model, [Eq. 4], which also considers the measured density of the material, were closer (average of 10% deviation) to the measured values in comparison to the Malis-Egerton model [Eq.2] (average of 27% deviation) confirming that density is a better predictor of MFP in comparison to the atomic number.

In addition, except for TiO₂, all calculated Inelastic MFP values were consistently lower than the measured values. Meltzman *et al.* [27] also report a similar trend, thus suggesting that these models underestimate the Inelastic MFP.

The Inelastic MFP of electrons in low-κ SiOCH thin film was significantly higher than the predicted value from both models (>25% deviation for Iakoubovskii and >40% for Malis, for 200keV electrons). We assume that due to the structure of such oxides which include nanoscale pores, the density of the film extracted from XRR measurements was overestimated.
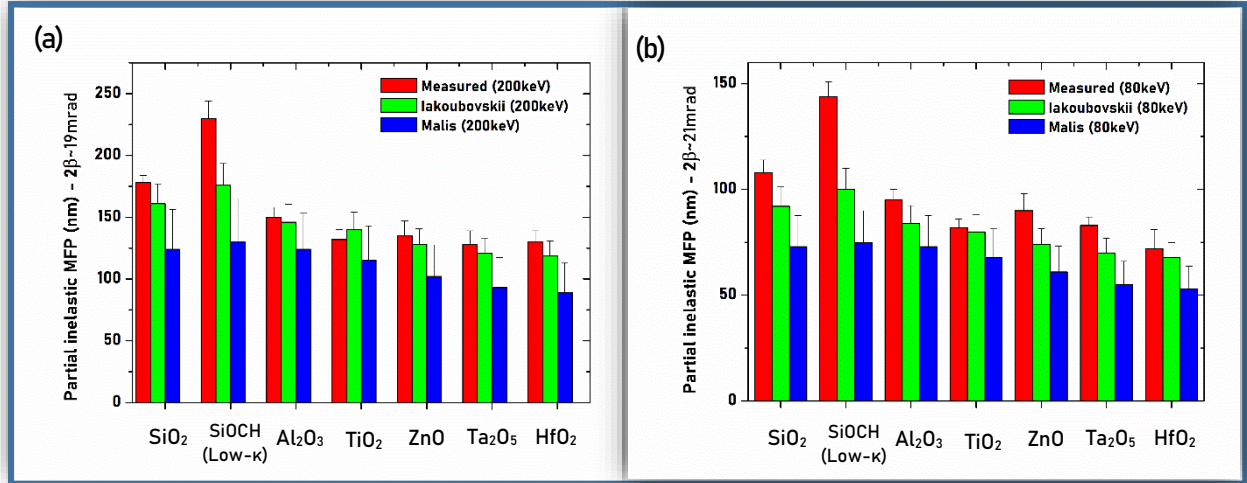
Figure 11. Measured vs calculated (Iakoubovskii[29] and Malis[18] models) partial Inelastic MFP values for (a) 200keV and (b) 80keV electrons in examined oxide thin films. The Inelastic MFP values were measured at a collection semi-angle of ~19mrad for 200keV and ~35mrad for 80keV (Objective aperture of 60μm diameter).

For 80keV electrons, we find a larger discrepancy between measured and calculated MFP values. This discrepancy can be expected considering that the Iakoubovskii model, [Eq.4], was developed empirically using measurements with 200keV electrons. The model suggests a simple relation for the Inelastic MFP with respect to density of $\lambda_{inelastic} \sim \rho^{-0.3}$ included into the Kramers-Kronig method and inelastic cross-section [29]. However, further studies by Iakoubovskii $et\ al.$ [37,52] show an oscillatory dependency of the Elastic and Inelastic MFP with atomic number.

Due to these relatively large deviations between calculated and measured Inelastic MFP values, we establish new correlations between the total Inelastic MFP and mass density for 200keV and 80keV electrons for the oxides studied here, covering a wide range of Z_{eff} and mass densities. These correlations were done by fitting of the measured total Inelastic MFP values to mass density, using a power law, incorporated into Iakoubovskii's model [29]. We note that the obtained relations apply equally well to all spectrometer collection angles.

We obtained a relation of $\lambda_{inelastic} \sim \rho^{-0.21\ \pm 0.017}$ and $\lambda_{inelastic} \sim \rho^{-0.17\ \pm 0.016}$ for 200keV and 80keV electrons, respectively, as shown in Fig.12. This result is consistent with our measured Inelastic MFP values while the predictions of the Iakoubovskii model were consistently lower [29].
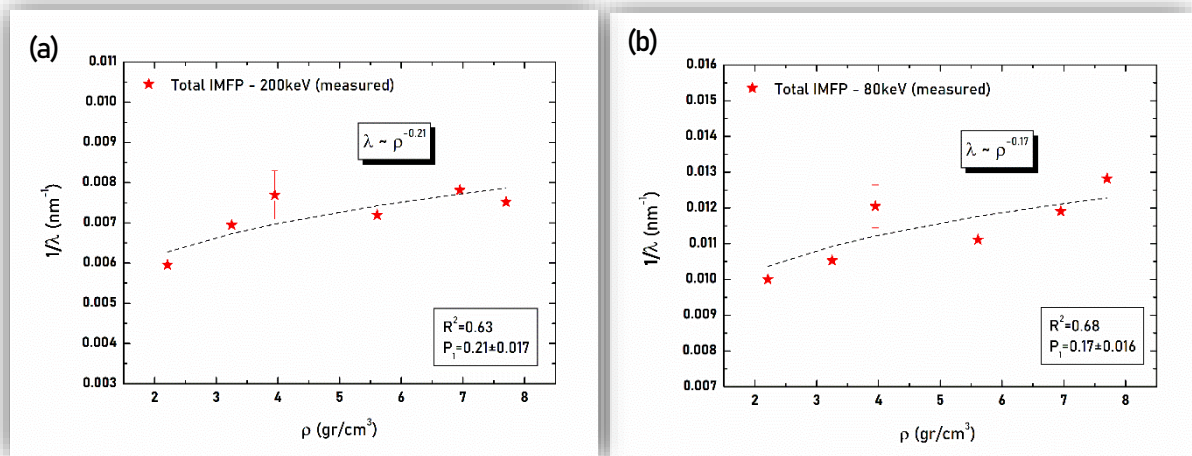

Figure 12. Fitting (dashed lines) of the measured total Inelastic MFP values to mass density, using a power law, as suggested by Iakoubovskii's model [29]. The same correlations to mass density were obtained for the various collection angles examined in this work.

14

3.2 Elastic MFP

The total Elastic MFP and elastic scattering cross-section, $\sigma_{elastic}$, for large collection angles can be calculated based on the Wenzel and Lenz models for elastic scattering according to [Eqs. 5,6] [28,38,53,54]:

$$\sigma_{elastic} = \frac{Z^2 R^2 \lambda^2 \left(1 + \frac{E}{E_0}\right)^2}{\pi a_H^2} \, [m^2] \tag{5}$$

$$\lambda_{elastic} = A/(N_0 \, \sigma_{el} \rho) \, [m] \tag{6}$$

Where Z is the atomic number, R is the effective atomic radius ($R = a_H Z^{-\frac{1}{3}}$), a_H is the Bohr radius (0.0529nm), λ is the incident electrons wavelength, E_0 is the electrons rest energy ($m_0 c^2$) = 0.511keV, E is the energy of the incident electrons ; N_0 is Avogadro's number, ρ and A are mass density and the average atomic mass of the material, respectively.

If the sample is a compound, then Z is replaced by an effective atomic number, Z_{eff}, according to [Eq. 7] for elastic scattering because experimental cross sections are reported to be closer to a $Z^{3/2}$ dependence [28,55].

$$Z_{eff} = \sqrt[3/2]{\sum_i f_i Z_i^{3/2}} \tag{7}$$

Where: f_i is the atomic fraction of element i in the material.

Fig.13 show the measured and calculated (Eq. 6) elastic MFP values for 200keV and 80keV electrons in the studied oxide thin films. The average deviation between measurement and model is ~20% and 33% for 200keV and 80keV electrons, respectively.
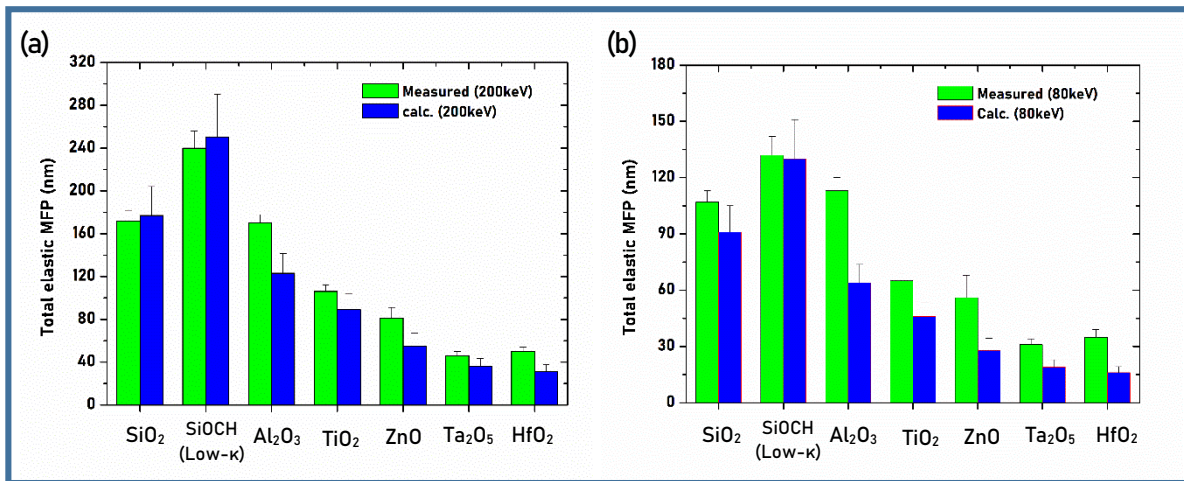

Figure 13. Total elastic MFP values, β~157mrad, (Wentzel model)[38] of (a) 200keV and (b) 80keV electrons in examined oxide thin films.

To improve the prediction accuracy for a selected range of atomic numbers of the studied oxides, we adopt a parametrized functional method of *Zhang et al.* [28] in which a generalized expression for the effective atomic radius is proposed [Eq.8] :

$$R = x_1 a_H Z^{x_2} \tag{8}$$

Where x_1 and x_2 are determined by fitting the measured Elastic MFP data using [Eq.9] which combines [Eqs.6 and 8]:

$$\lambda_{elastic} = \frac{A\pi}{N_0 \rho x_1 \lambda^2 \left(1 + \frac{E}{E_0}\right)^2 Z_{eff}^{2(1+x_2)}} \tag{9}$$

Fig. 14 show a linear regression fitting of log-log plot of the $\frac{\lambda_{elastic}\rho}{A}$ data as a function of the Z_{eff} for 200keV and 80keV electrons for the examined oxide thin films. $\lambda_{elastic}$ is the measured total elastic MFP values; ρ and A are the mass density $[\frac{gr}{cm^3}]$ and average molar mass $[\frac{gr}{mol}]$, respectively.

The intercept and slope for each electron energy are shown in the inset. Hence our proposed Elastic MFP relations for oxides are [Eq.10] and [Eq.11] for 200keV and 80keV electrons, respectively:

$$\lambda_{elastic}(nm) = \frac{10^4 * Ae^{-3.41}}{\rho} Z_{eff}^{-1.15} \quad \text{(For 200keV electrons)} \tag{10}$$

$$\lambda_{elastic}(nm) = \frac{10^4 * Ae^{-4}}{\rho} Z_{eff}^{-1.08} \quad \text{(For 80keV electrons)} \tag{11}$$
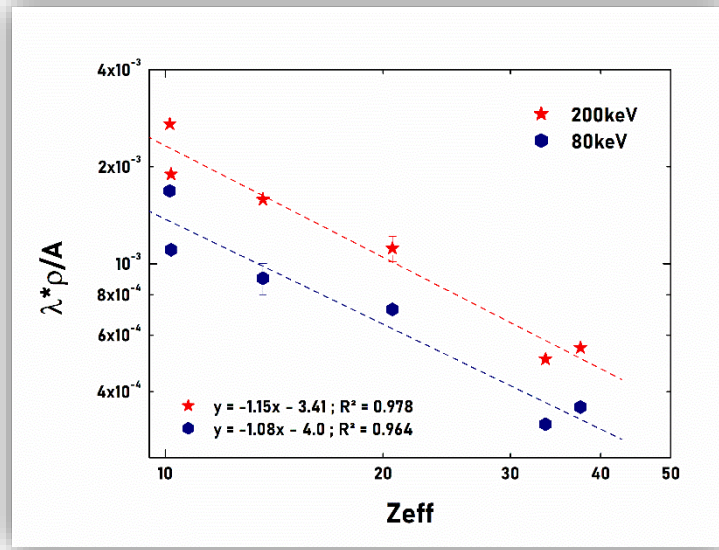

Figure 14. Linear regression fitting of log-log plot of measured $\frac{\lambda_{elastic}\rho}{A}$ as a function of the Z_{eff} for 200keV and 80keV electrons in the examined oxide thin films.

4. Inelastic to Elastic MFP ratio

The Inelastic to Elastic MFP ratio is important for determining optimal sample thickness for structural characterization of amorphous thin films such as short-range order [34]. In addition, modeling this ratio as a function of atomic number can be used to estimate the mean atomic number of the examined material or to estimate the dominant mechanism for radiation damage due to the electron beam, namely atom displacement or radiolysis [35,36].

The ratio of Inelastic to Elastic MFP can be estimated using an empirical relation [53], which is proportional to the atomic number of the material, $Z/20$. Accordingly, we would expect elastic scattering to be the less dominant process in oxides such as SiO_2 with $Z_{eff} \sim 10$ in comparison to a more significant elastic scattering component in oxides such as Ta_2O_5 with $Z_{eff} \sim 33$.

The total Inelastic MFP measured at a collection semi-angle of $\beta \sim 157$ mrad was compared to the total Elastic MFP in all oxide thin films for both electron energies. This is shown for an example in Fig. 15 for thermal SiO_2 and Ta_2O_5.
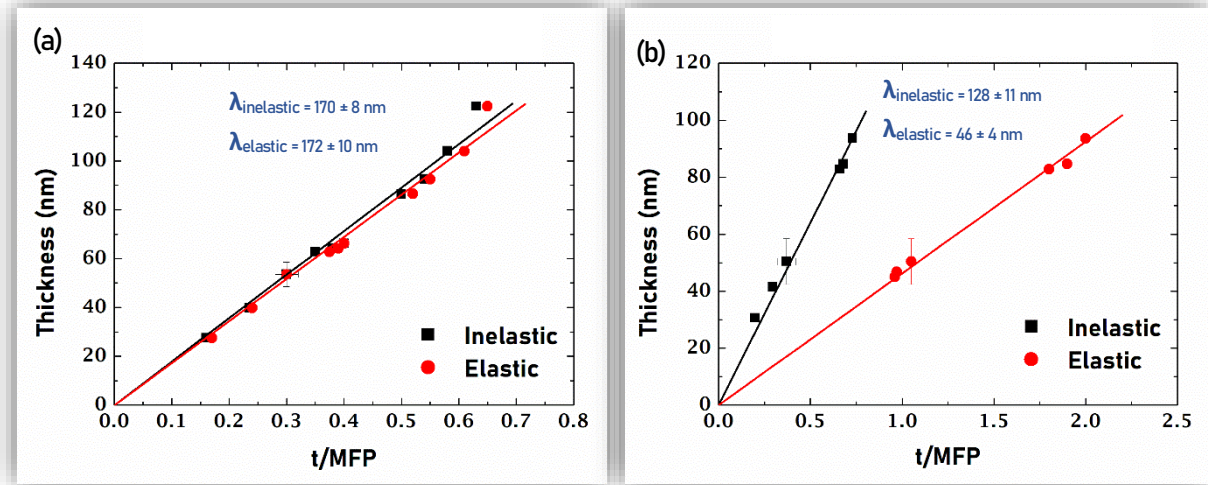

Figure 15. Thickness of the TEM sample in the region of (a) thermal SiO_2 and (b) Ta_2O_5 thin films at different locations across each sample as a function of the measured t/EMFP and t/IMFP (200keV electrons, $\beta \sim 157$mrad). The total MFP values were extracted from each slope and highlighted in each of the plots.

The Inelastic MFP to Elastic MFP ratio for all oxide thin films as a function of the effective atomic number (Z_{eff}) and density (ρ) are shown in Fig. 16.

For oxides with smaller Z_{eff}, such as SiO_2 and Al_2O_3, the $\lambda_{inelastic} / \lambda_{elastic}$ ratio approaches 1, while oxides with large Z_{eff} such as HfO_2 and Ta_2O_5 exhibit significantly larger $\lambda_{inelastic} / \lambda_{elastic}$ ratios, approaching 2.5.

As expected, for larger Z_{eff} and ρ, we measure a decrease in the Elastic MFP in comparison to the Inelastic MFP, suggesting that elastic scattering is the more dominant event for heavier oxides. The measured Inelastic MFP to Elastic MFP ratio for oxides is parameterized in [Eq.12] and [Eq.13] for 200keV and 80keV electrons, respectively.

17

$$\frac{\lambda_{inelastic}\ (measured)}{\lambda_{elastic}(measured)} \approx \frac{Zeff}{16} \text{ (For 200keV electrons)} \tag{12}$$

$$\frac{\lambda_{inelastic}\ (measured)}{\lambda_{elastic}(measured)} \approx \frac{Zeff}{17} \text{ (For 80keV electrons)} \tag{13}$$
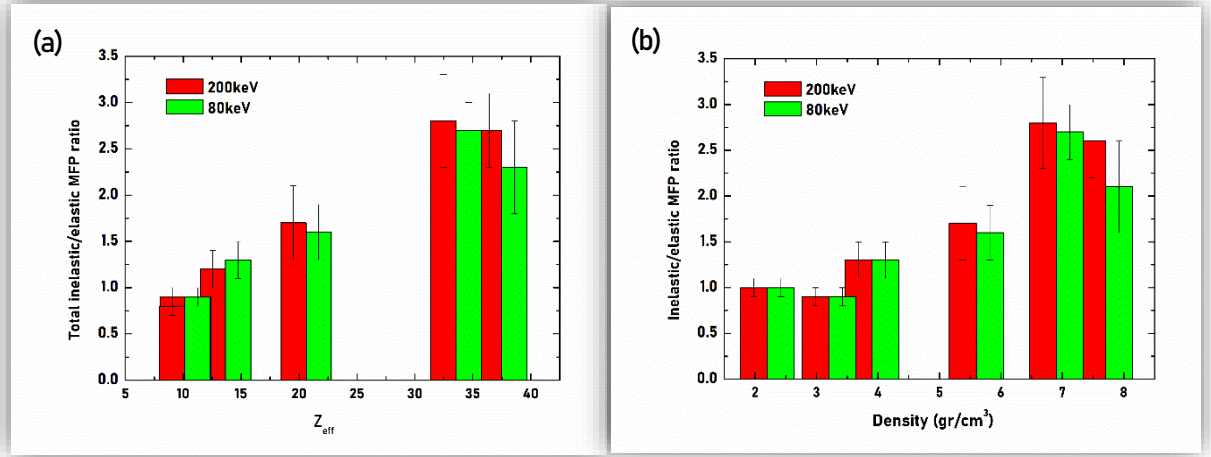

Figure 16. Total inelastic to Elastic MFP ratio for 200keV and 80keV electrons as a function of (a) the effective atomic number (Z_{eff}) and (b) the mass density, ρ.

We propose an additional experimental relation for the Elastic/Inelastic MFP ratio using the density, in units of ($\frac{gr}{cm^3}$), of the oxide, as expressed in [Eq.14] and [Eq.15] for 200keV and 80keV electrons, respectively. This model can be used for estimating Inelastic/Elastic MFP ratio of oxides for the density range of $2.2 - 7.7(\frac{gr}{cm^3})$. The low-κ SiOCH was not included in the development of [Eqs.10-15] due to its complex composition and porosity which warrants a separate study.

$$\frac{\lambda_{inelastic}\ (measured)}{\lambda_{elastic}(measured)} \approx \frac{\rho}{2.7} \text{ (For 200keV electrons)} \tag{14}$$

$$\frac{\lambda_{inelastic}\ (measured)}{\lambda_{elastic}(measured)} \approx \frac{\rho}{3.1} \text{ (For 80keV electrons)} \tag{15}$$

Summary

We measured the Elastic and Inelastic Mean Free Paths for 200keV and 80keV electrons in technologically important oxide thin-films: SiO_2 (Thermal, CVD), low-κ SiOCH, Al_2O_3, TiO_2, ZnO, Ta_2O_5 and HfO_2.

The MFP values were measured using the log-ratio method applied to EF-TEM and BF TEM images, combined with a wedge TEM sample preparation technique. The actual thicknesses of the samples were calibrated using the Inelastic MFP of the crystalline Si substrate as a function of electron energy and collection semi-angle (Table 1, e.g., total Inelastic MFP for 200 keV electrons of 145 ± 10nm).

The measured total Elastic and Inelastic MFP values of the examined oxides are presented in Tables 2 and 3, respectively. The measured Inelastic MFP values as a function of collection semi-angles are presented in Fig. 8c, and Fig. 9.

Comparison of model data to the experimental measurements show that the Iakobouskii's approach [26] is more accurate (10% average deviation) compared to the Malis approach (>27% deviation) for 200keV electrons [18]. Calculated MFP values based on both approaches were consistently lower than the measured values, with the exception of TiO_2.

Based on our measurements, we propose a modified function of the mass density incorporated into the Iakoubovskii Inelastic MFP relation, which achieves improved accuracy for oxides: $\lambda_{inelastic} \sim \rho^{-0.21\,\pm0.017}$ and $\lambda_{inelastic} \sim \rho^{-0.17\,\pm0.016}$ for 200keV and 80keV electrons, respectively. These new relations reduce the average deviation from experimental measurements to ~5% in comparison to the larger deviation of the Iakoubovskii model (~10% and 17% for 200keV and 80keV electrons, respectively). Furthermore, we propose a more accurate model for Elastic MFPs of oxides, Eqs. [10,11] for 200keV and 80keV electrons, respectively, which results in lower average deviations from measurements of ~10% and 15% in comparison to the Wenzel model, ~20% and 33%.

We examined the ratio of Elastic to Inelastic MFP in oxides, which is important for structural characterization [34] and for assessing electron beam radiation damage [35]. The total Elastic to Inelastic MFP ratios for 200keV and 80keV electrons were fitted to the effective atomic number, Z_{eff}, as $\approx \frac{Zeff}{16}$ and $\approx \frac{Zeff}{17}$, respectively; and to the mass density (ρ, gr/cm^3) as $\approx \frac{\rho}{2.7}$ and $\approx \frac{\rho}{3.1}$, respectively. These relations do not include the low-κ SiOCH due to its porous structure which requires a separate study.

Acknowledgements

References

[1]   A. Kohn, A. Kovács, T. Uhrmann, T. Dimopoulos, H. Brückl, Structural and electrical characterization of SiO_2/MgO(001) barriers on Si for a magnetic transistor, Appl. Phys. Lett. 95 (2009) 42506. https://doi.org/10.1063/1.3182732.

[2]   E. Fortunato, P. Barquinha, R. Martins, Oxide Semiconductor Thin-Film Transistors: A Review of Recent Advances, Adv. Mater. 24 (2012) 2945–2986. https://doi.org/10.1002/ADMA.201103228.

[3]   T.-J. Lee, S.-K. Kim, T.-Y. Seong, Sputtering-deposited amorphous SrVOx-based memristor for use in neuromorphic computing, Sci. Rep. 10 (2020) 5761. https://doi.org/10.1038/s41598-020-62642-3.

[4]   R. Bassiri, K.B. Borisenko, D.J.H. Cockayne, J. Hough, I. MacLaren, S. Rowan, Probing the atomic structure of amorphous Ta_2O_5 coatings, Appl. Phys. Lett. 98 (2011). https://doi.org/10.1063/1.3535982.

[5]   K. Umeda, M. Uenuma, D. Senaha, J.C. Felizco, Y. Uraoka, H. Adachi, Amorphous Thin Film for Thermoelectric Application, J. Phys. Conf. Ser. 1052 (2018). https://doi.org/10.1088/1742-6596/1052/1/012016.

[6]   S. Vizzini, H. Oughaddou, C. Léandri, V.K. Lazarov, A. Kohn, K. Nguyen, C. Coudreau, J.P. Bibérian, B. Ealet, J.L. Lazzari, F. Arnaud d'Avitaya, B. Aufray, Controlled growth of aluminum oxide thin films on hydrogen terminated Si(0 0 1) surface, J. Cryst. Growth. 305 (2007) 26–29. https://doi.org/10.1016/J.JCRYSGRO.2007.03.037.

[7]   J.H. Ryu, F. Hussain, C. Mahata, M. Ismail, Y. Abbas, M.H. Kim, C. Choi, B.G. Park, S. Kim, Filamentary and interface switching of CMOS-compatible Ta_2O_5 memristor for non-volatile memory and synaptic devices, Appl. Surf. Sci. 529 (2020). https://doi.org/10.1016/J.APSUSC.2020.147167.

[8]   A.N. Rodrigues, Y.P. Santos, C.L. Rodrigues, M.A. Macêdo, Al_2O_3 thin film multilayer structure for application in RRAM devices, Solid. State. Electron. 149 (2018) 1–5. https://doi.org/10.1016/J.SSE.2018.08.004.

[9]   T. Kim, H. Son, I. Kim, J. Kim, S. Lee, J. Keuk Park, Y. Kwak, J. Park, Y. Jeong, Reversible switching mode change in Ta_2O_5-based resistive switching memory (ReRAM), Sci. Rep. 10 (2020) 11247. https://doi.org/10.1038/s41598-020-68211-y.

[10]   J. Robertson, R.M. Wallace, High-K materials and metal gates for CMOS applications, Mater. Sci. Eng. R Reports. 88 (2015) 1–41. https://doi.org/10.1016/J.MSER.2014.11.001.

[11]   T.E. Gorelik, R. Neder, M.W. Terban, Z. Lee, X. Mu, C. Jung, T. Jacob, U. Kaiser, Towards quantitative treatment of electron pair distribution function, Acta Crystallogr. Sect. B Struct. Sci. Cryst. Eng. Mater. 75 (2019) 532–549. https://doi.org/10.1107/S205252061900670X.

[12]   D.J.H. Cockayne, The study of nanovolumes of amorphous materials using electron scattering, Annu. Rev. Mater. Res. 37 (2007) 159–187. https://doi.org/10.1146/annurev.matsci.35.082803.103337.

[13]   K.J. Ganesh, M. Kawasaki, J.P. Zhou, P.J. Ferreira, D-STEM: A parallel electron diffraction technique applied to nanomaterials, Microsc. Microanal. 16 (2010) 614–621. https://doi.org/10.1017/S1431927610000334.

[14]   K. Oh-ishi, T. Ohsuna, Inelastic mean free path measurement by STEM-EELS technique using needle-shaped specimen, Ultramicroscopy. 212 (2020) 112955. https://doi.org/10.1016/j.ultramic.2020.112955.

[15]   C.W. Lee, Y. Ikematsu, D. Shindo, Measurement of mean free paths for inelastic electron scattering of Si and SiO_2, J. Electron Microsc. (Tokyo). 51 (2002) 143–148. https://doi.org/10.1093/jmicro/51.3.143.

[16]   P.L. Potapov, The experimental electron mean-free-path in Si under typical (S)TEM conditions, Ultramicroscopy. 147 (2014) 21–24. https://doi.org/10.1016/j.ultramic.2014.05.010.

[17]   Y.Y. Yang, R.F. Egerton, Tests of two alternative methods for measuring specimen thickness in a transmission electron microscope, Micron. 26 (1995) 1–5. https://doi.org/10.1016/0968-4328(94)00039-S.

[18]   T. Malis, S.C. Cheng, R.F. Egerton, EELS log-ratio technique for specimen-thickness measurement in

the TEM, J. Electron Microsc. Tech. 8 (1988) 193–200. https://doi.org/10.1002/jemt.1060080206.

[19]   J. Berriman, R.K. Bryan, R. Freeman, K.R. Leonard, Methods for specimen thickness determination in electron microscopy, Ultramicroscopy. 13 (1984) 351–364. https://doi.org/10.1016/0304-3991(84)90001-9.

[20]   Z. Pan, C.K.L. Davies, R.N. Stevens, Measurement of foil thickness in transmission electron microscopy, J. Mater. Sci. 29 (1994) 1920–1924. https://doi.org/10.1007/BF00351314.

[21]   S.M. Allen, E.L. Hall, Foil thickness measurements from convergent-beam diffraction patterns An experimental assessment of errors, Philos. Mag. A. 46 (1982) 243–253. https://doi.org/10.1080/01418618208239917.

[22]   P.M. Kelly, A. Jostsons, R.G. Blake, J.G. Napier, The determination of foil thickness by scanning transmission electron microscopy, Phys. Status Solidi. 31 (1975) 771–780. https://doi.org/10.1002/PSSA.2210310251.

[23]   D.R.G. Mitchell, Determination of mean free path for energy loss and surface oxide film thickness using convergent beam electron diffraction and thickness mapping: A case study using Si and P91 steel, J. Microsc. 224 (2006) 187–196. https://doi.org/10.1111/J.1365-2818.2006.01690.X.

[24]   D.T. Schweiss, J. Hwang, P.M. Voyles, Inelastic and elastic mean free paths from FIB samples of metallic glasses, Ultramicroscopy. 124 (2013) 6–12. https://doi.org/10.1016/j.ultramic.2012.08.005.

[25]   J. Ghatak, A. Chatterjee, S.M. Shivaprasad, Site-specific angular dependent determination of inelastic mean free path of 300 keV electrons in GaN nanorods, J. Microsc. 282 (2021) 250–257. https://doi.org/10.1111/jmi.12999.

[26]   H.-R. Zhang, R.F. Egerton, M. Malac, Local thickness measurement through scattering contrast and electron energy-loss spectroscopy, Micron. 43 (2012) 8–15. https://doi.org/10.1016/j.micron.2011.07.003.

[27]   H. Meltzman, Y. Kauffmann, P. Thangadurai, M. Drozdov, M. Baram, D. Brandon, W.D. Kaplan, An experimental method for calibration of the plasmon mean free path, J. Microsc. 236 (2009) 165–173. https://doi.org/10.1111/J.1365-2818.2009.03214.X.

[28]   P. Zhang, Z. Wang, J.H. Perepezko, P.M. Voyles, Elastic and inelastic mean free paths of 200 keV electrons in metallic glasses, Ultramicroscopy. 171 (2016) 89–95. https://doi.org/10.1016/j.ultramic.2016.09.005.

[29]   K. Iakoubovskii, K. Mitsuishi, Y. Nakayama, K. Furuya, Thickness measurements with electron energy loss spectroscopy, Microsc. Res. Tech. 71 (2008) 626–631. https://doi.org/10.1002/jemt.20597.

[30]   M.N. Yesibolati, S. Laganá, S. Kadkhodazadeh, E.K. Mikkelsen, H. Sun, T. Kasama, O. Hansen, N.J. Zaluzec, K. Mølhave, Electron inelastic mean free path in water, Nanoscale. 12 (2020) 20649–20657. https://doi.org/10.1039/D0NR04352D.

[31]   A. Pantzer, A. Vakahy, Z. Eliyahou, G. Levi, D. Horvitz, A. Kohn, Dopant mapping in thin FIB prepared silicon samples by Off-Axis Electron Holography, Ultramicroscopy. 138 (2014) 36–45. https://doi.org/10.1016/j.ultramic.2013.12.001.

[32]   N. Ni, S. Lozano-Perez, J. Sykes, C. Grovenor, Quantitative EELS analysis of zirconium alloy metal/oxide interfaces, Ultramicroscopy. 111 (2011) 123–130. https://doi.org/10.1016/j.ultramic.2010.10.020.

[33]   A. Varambhia, L. Jones, A. London, D. Ozkaya, P.D. Nellist, S. Lozano-Perez, Determining EDS and EELS partial cross-sections from multiple calibration standards to accurately quantify bi-metallic nanoparticles using STEM, Micron. 113 (2018) 69–82. https://doi.org/10.1016/j.micron.2018.06.015.

[34]   D. Cockayne, Y. Chen, G. Li, K. Borisenko, The technique of RDF of nanovolumes using electron diffraction, J. Phys. Conf. Ser. 241 (2010). https://doi.org/10.1088/1742-6596/241/1/012006.

[35]   R.F. Egerton, P. Li, M. Malac, Radiation damage in the TEM and SEM, Micron. 35 (2004) 399–409. https://doi.org/10.1016/j.micron.2004.02.003.

[36] R.F. Egerton, Measurement of inelastic/elastic scattering ratio for fast electrons and its use in the study of radiation damage, Phys. Status Solidi. 37 (1976) 663–668. https://doi.org/10.1002/pssa.2210370237.

[37] K. Iakoubovskii, K. Mitsuishi, Y. Nakayama, K. Furuya, Mean free path of inelastic electron scattering in elemental solids and oxides using transmission electron microscopy: Atomic number dependent oscillatory behavior, Phys. Rev. B. 77 (2008) 104102. https://doi.org/10.1103/PhysRevB.77.104102.

[38] F. Lenz, Zur Streuung mittelschneller Elektronen in kleinste Winkel, Zeitschrift Fur Naturforsch. - Sect. A J. Phys. Sci. 9 (1954) 185–204. https://doi.org/10.1515/zna-1954-0301.

[39] D. Miron, I. Krylov, M. Baskin, Understanding leakage currents through Al_2O_3 on $SrTiO_3$ COLLECTIONS ARTICLES YOU MAY BE INTERESTED IN, J. Appl. Phys. 126 (2019) 185301. https://doi.org/10.1063/1.5119703.

[40] G.D. Liechty, E. Hirsch, C.A. Smith, MultiPrep^{TM} Procedure TEM Wedge Preparation of an Integrated Circuit (IC), 2003.

[41] X. Mu, A. Mazilkin, C. Sprau, A. Colsmann, C. Kübel, Mapping structure and morphology of amorphous organic thin films by 4D-STEM pair distribution function analysis, Microscopy. 68 (2019) 301–309. https://doi.org/10.1093/jmicro/dfz.

[42] K.A. Jackson, Silicon devices : structures and processing, Wiley-VCH, weinheim, Germany, 1998.

[43] G. Li, S. Shittu, T.M.O. Diallo, M. Yu, X. Zhao, J. Ji, A review of solar photovoltaic-thermoelectric hybrid system for electricity generation, Energy. 158 (2018) 41–58. https://doi.org/10.1016/j.energy.2018.06.021.

[44] A. Hosseini, H.H. Güllü, E. Coskun, M. Parlak, C. Ercelebi, Fabrication and Characterization of TiO2 Thin Film For Device Applications, 26 (2019). https://doi.org/10.1142/S0218625X18502050.

[45] J. Lu, J. Aarik, J. Sundqvist, K. Kukli, A. Hårsta, J.O. Carlsson, Analytical TEM characterization of the interfacial layer between ALD HfO_2 film and silicon substrate, J. Cryst. Growth. 273 (2005) 510–514. https://doi.org/10.1016/j.jcrysgro.2004.09.064.

[46] J.M. Khoshman, M.E. Kordesch, Optical properties of a-HfO_2 thin films, Surf. Coatings Technol. 201 (2006) 3530–3535. https://doi.org/10.1016/J.SURFCOAT.2006.08.074.

[47] W.-C. Shih, T.-L. Wang, M.-H. Chu, Characteristics of ZnO Thin Film Surface Acoustic Wave Devices Fabricated Using Al_2O_3 Films on Silicon Substrates, Jpn. J. Appl. Phys. 49 (2010) 07HD19. https://doi.org/10.1143/jjap.49.07hd19.

[48] Q. Jin, Thickness Measurements of a TEM Foil and Its Surface Layer By Electron Energy-Loss Spectroscopy, Microsc. Microanal. 10 (2004) 882–883. https://doi.org/10.1017/S1431927604881327.

[49] C.W. Lee, Y. Ikematsu, D. Shindo, Thickness measurement of amorphous SiO_2 by EELS and electron holography, Mater. Trans. JIM. 41 (2000) 1129–1131. https://doi.org/10.2320/matertrans1989.41.1129.

[50] H. Shinotsuka, S. Tanuma, C.J. Powell, D.R. Penn, Calculations of electron inelastic mean free paths. XII. Data for 42 inorganic compounds over the 50 eV to 200 keV range with the full Penn algorithm We have calculated inelastic mean free paths (IMFPs) for 42 inorganic compounds, (2018). https://doi.org/10.1002/sia.6598.

[51] R.F. Egerton, S.C. Cheng, Measurement of local thickness by electron energy-loss spectroscopy, Ultramicroscopy. 21 (1987) 231–244. https://doi.org/10.1016/0304-3991(87)90148-3.

[52] K. Iakoubovskii, K. Mitsuishi, Elastic scattering of 200keV electrons in elemental solids: Experimental observation of atomic-number-dependent oscillatory behavior, J. Phys. Condens. Matter. 21 (2009). https://doi.org/10.1088/0953-8984/21/15/155402.

[53] H. Reimer, L., & Kohl, Transmission electron microscopy: Physics of image formation., 5th ed., Springer US, New York, NY, 2008. https://doi.org/10.1007/978-0-387-40093-8.

[54] D.B. Williams, C.B. Carter, The Transmission Electron Microscope, in: Transm. Electron Microsc. A Textb. Mater. Sci., Springer US, Boston, MA, 1996: pp. 3–17. https://doi.org/10.1007/978-1-4757-

2519-3_1.

[55] J.P. Langmore, J. Wall, M.S. Isaacson, Collection of Scattered Electrons in Dark Field Electron Microscopy - 1. Elastic Scattering, Opt. 38 (1973) 335–350.

Supplementary Information

Calibration of the collection semi-angle, β

The EEL spectrometer collection semi-angle, β , is determined by the objective aperture. An example for the calibration of the angular diameter of the objective apertures using electron diffraction patterns from the underlying silicon substrate is shown in Fig. S1. The measured collection semi-angles β were in the range between 2 and 157 mrad as summarized in Table S1. A collection semi-angle of β~157 mrad applies to the removal of the objective apertures, such that the angle is limited by the objective lens bore [36] or the differential pumping aperture (between the viewing chamber and the projector lens) of the JEOL JEM 2010F TEM [23].
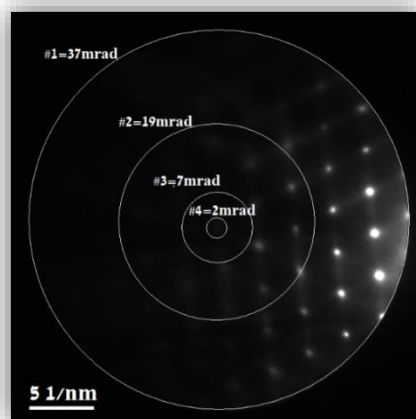

Figure S1. TEM selected area diffraction pattern from the crystalline silicon (001) substrate, oriented to [110] zone axis. The schematic rings represent the objective apertures #1-4 and their respective angular diameter.

Table S1. Angular diameter (mrad) of objective apertures measured at 200 and 80kV acceleration voltage				
	Measured collection semi-angle β (mrad)			
Acc. Voltage	Objective Ap. #1 Diameter = 120μm	Objective Ap. #2 Diameter = 60μm	Objective Ap. #3 Diameter = 20μm	Objective Ap. #4 Diameter = 5μm
200 kV	36 ± 1	19 ± 1	6.7 ± 0.5	2 ± 0.5
80 kV	69 ± 2	35 ± 1	12.1 ± 0.5	3.5 ± 0.5

Composition of oxides - X-ray Photoelectron Spectroscopy

Calculated MFP values using the Wentzel and Iakoubovskii models for elastic and inelastic scattering, respectively, both require the composition, namely the effective atomic number, Z_{eff}, and the mass density, ρ, of each material. The composition of each oxide thin-film was determined using the ratio between the different oxidation states shown in the deconvoluted XPS spectra. For example, Fig. S2 show deconvoluted high energy-resolution XPS spectra of the TiO_2 thin-film. The intensity ratio between the Ti^{3+} and the Ti^{4+} oxidation state peaks is ~ (4.6:1), hence the estimated composition of the film is $TiO_{1.9}$. The measured elemental ratio of the studied oxide thin films is summarized in Table S2.
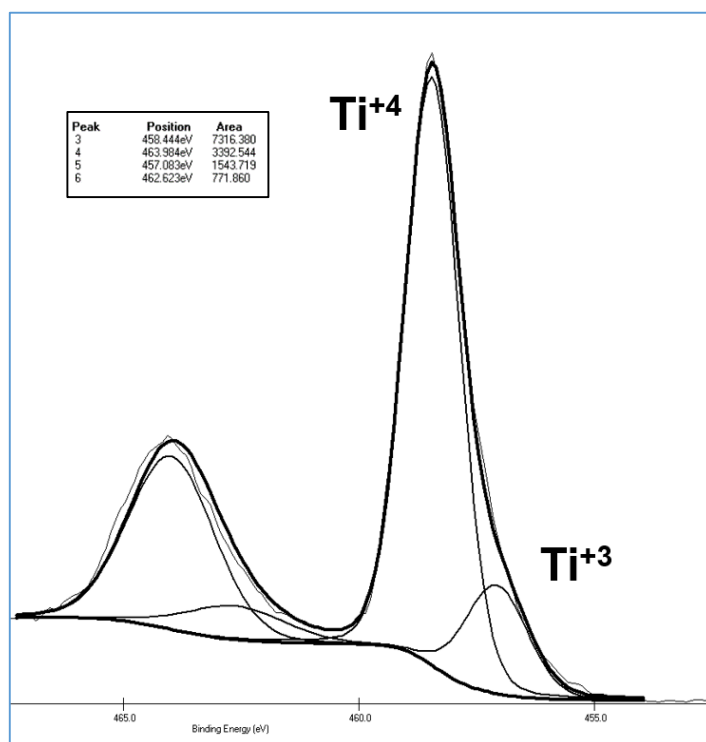
Figure S2. XPS high energy-resolution spectra of Ti 2p binding energy acquired from the TiO_2 thin-film sample. The area under the curve (total peak intensities) for each of the deconvoluted peaks is shown in the inset. The measured intensities enable calculation of the oxidation states ratios and the average film composition.

Table S2. Measured elemental ratio of the studied oxide thin films

Oxide	TiO_2	HfO_2	ZnO	Ta_2O_5	Al_2O_3	SiO_2(thermal)	SiO_2(CVD)	SiOCH (Low-κ)
Elemental ratio	Ti:O 1:1.9	Hf:O 1:1.9	Zn:O 1:1	Ta:O 2:5	Al:O 2:3	Si:O 1:2	Si:O 1:2	Si:O:C 1:2:1

Mass density – X-ray Reflectivity

The mass density of the oxide thin films was determined using XRR measurements. This was executed using fitting softwares (Global fit 2.0 and SmartLab studio II by Rigaku) as shown for example for TiO_2 in Fig. S3.
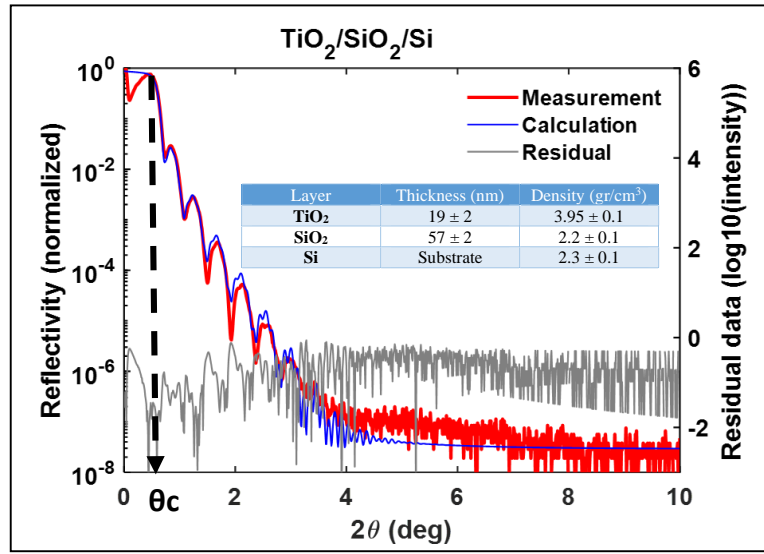
Figure S3. Measured and calculated normalized X-ray reflectivity vs total reflection angle (2θ) acquired from a TiO$_2$/SiO$_2$/Si sample. Inset table summarizes the film thickness and density values that yield the best fit for the critical reflection angle and the X-ray reflection oscillations.

Experimental errors in determining the MFP from the log ratio approach

Experimental errors for [Eqs.1a and 1b] may result due to several factors, such as [36]:

(a) Scattered electrons that do not reach the detector (limited angular range of the detector).

(b) Small angle elastically scattered electrons that enter the 2mrad objective aperture.

(c) Inelastically scattered electrons that enter the energy selecting slit.

We estimate of the experimental errors based on the Wenzel model for elastic scattering:

$$\frac{\sigma e(\alpha)}{\sigma e} = (1 + q^{-2}R^{-2})^{-1} \qquad (S1)$$

Where $\sigma e(\alpha)$ is the scattering cross-section up to the collection angle (α), $q = \frac{4\pi}{\lambda}\sin\left(\frac{\alpha}{2}\right)$, λ is the electron wavelength, $R = a/Z^{\frac{1}{3}}$ is the Bohr radius and Z is the effective atomic number of the compound.

The expected errors due to factor (a) for each Z_{eff} for 200keV and 80keV electrons, in this case, α is the objective lens bore (semi-angle of ~157mrad) is summarized in Table S3:

Table S3

Zeff	200keV	80keV
10.14	1%	3%
13.64	1.30%	3.50%
20.60	1.70%	4.50%
33.55	2.30%	6%
37.50	2.50%	6.50%

The expected errors due to factor (b) for each Z_{eff} for 200keV and 80keV electrons, in this case, α is the smallest available objective aperture of ~2mrad for 200kV and ~3.5mrd for 80kV, is summarized in Table S4:

Table S4

Zeff	200keV	80keV
10.14	1.50%	1.60%
13.64	1.20%	1.35%
20.60	0.95%	1.00%
33.55	0.67%	0.75%
37.50	0.63%	0.69%